Low-Temperature Photophysics of Single Nitrogen-Vacancy Centers in Diamond

Jodok Happacher,[1] David A. Broadway,[1] Juanita Bocquel,[1] Patrick Reiser,[1] Alejandro Jimenéz,[2] Märta A. Tschudin,[1] Lucas Thiel,[1] Dominik Rohner,[1] Marcel. li Grimau Puigibert,[1] Brendan Shields,[1] Jeronimo R. Maze,[2] Vincent Jacques,[3] and Patrick Maletinsky[1,*]

[1]*Department of Physics, University of Basel, Klingelbergstrasse 82, Basel CH-4056, Switzerland*
[2]*Facultad de Física, Pontificia Universidad Católica de Chile, Santiago 7820436, Chile*
[3]*Laboratoire Charles Coulomb, Université de Montpellier and CNRS, 34095 Montpellier, France*

(Received 12 May 2021; revised 17 December 2021; accepted 18 February 2022; published 29 April 2022)

We investigate the magnetic field dependent photophysics of individual nitrogen-vacancy (NV) color centers in diamond under cryogenic conditions. At distinct magnetic fields, we observe significant reductions in the NV photoluminescence rate, which indicate a marked decrease in the optical readout efficiency of the NV's ground state spin. We assign these dips to excited state level anticrossings, which occur at magnetic fields that strongly depend on the effective, local strain environment of the NV center. Our results offer new insights into the structure of the NVs' excited states and a new tool for their effective characterization. Using this tool, we observe strong indications for strain-dependent variations of the NV's orbital g factor, obtain new insights into NV charge state dynamics, and draw important conclusions regarding the applicability of NV centers for low-temperature quantum sensing.

DOI: 10.1103/PhysRevLett.128.177401

The nitrogen-vacancy (NV) lattice defect in diamond [1] hosts a versatile solid state spin system that finds applications in quantum metrology [2], nanoscale imaging [3], or quantum information processing [4]. In these, the NV spin stands out due to its excellent quantum coherence properties, which persist across a wide range of temperatures [5] and pressures [6]. As a result of their performance and robustness, NV spins have been employed in practical applications ranging from remote spin-spin entanglement [7] to nanoscale magnetic imaging [3,8], even under cryogenic conditions [9,10].

The majority of such applications build on methods for efficient optical NV spin initialization [11,12] and readout [13,14]—two key features that result from properties of the NV's orbital excited states. At temperatures $T \gtrsim 100$ K, orbital averaging allows for a description of the NV excited states as an effective spin-one system, with spin states $|-1\rangle$, $|0\rangle$, and $|1\rangle$, characterized by the magnetic quantum number along the nitrogen-vacancy axis [15,16]. Initialization and readout of the NV's ground-state spin-one system then result from optical transitions being largely spin conserving for $|0\rangle$, while excited state spin levels $|\pm 1\rangle$ show a nonradiative intersystem crossing into NV spin singlet states, followed by relaxation into the NV triplet ground state [1].

At cryogenic temperatures, however, this effective spin-one description of the NV excited states does not hold, since orbital averaging slows down and becomes negligible at temperatures $T \lesssim 20$ K [15,16]. The question how the emerging and rich orbital excited state structure affects the NV's photophysical properties is of relevance to most low-temperature experiments on NV spins, but has received remarkably little attention thus far. Previous work on NV ensembles has already attributed variations of NV photoluminescence (PL) with magnetic field to mixing of the excited states, but a complete picture was obscured by ensemble averaging [17]. Conversely, for single NVs, only the regime near zero magnetic field and few fixed higher field values have been explored thus far [16,18]. At the same time, consistent observations of significant reductions in NV PL and spin-readout contrast have been made in the context of low-temperature NV magnetometry [10,19], but remain unexplained up to now.

To address these questions, we present a systematic study of the photophysical properties of individual NV centers at cryogenic temperatures. Specifically, we study the dependence of the NV PL rate on static magnetic fields, B_{NV}, applied along the NV axis. We observe significant PL reductions, at well-defined, strain-dependent values of B_{NV}, that we assign to NV excited state level anticrossings (ESLACs), which result in efficient NV spin mixing and subsequent intersystem crossings. The B_{NV} values where the ESLACs occur further allow for an extraction of the NV's orbital g factor, g_l. Interestingly, we find previously

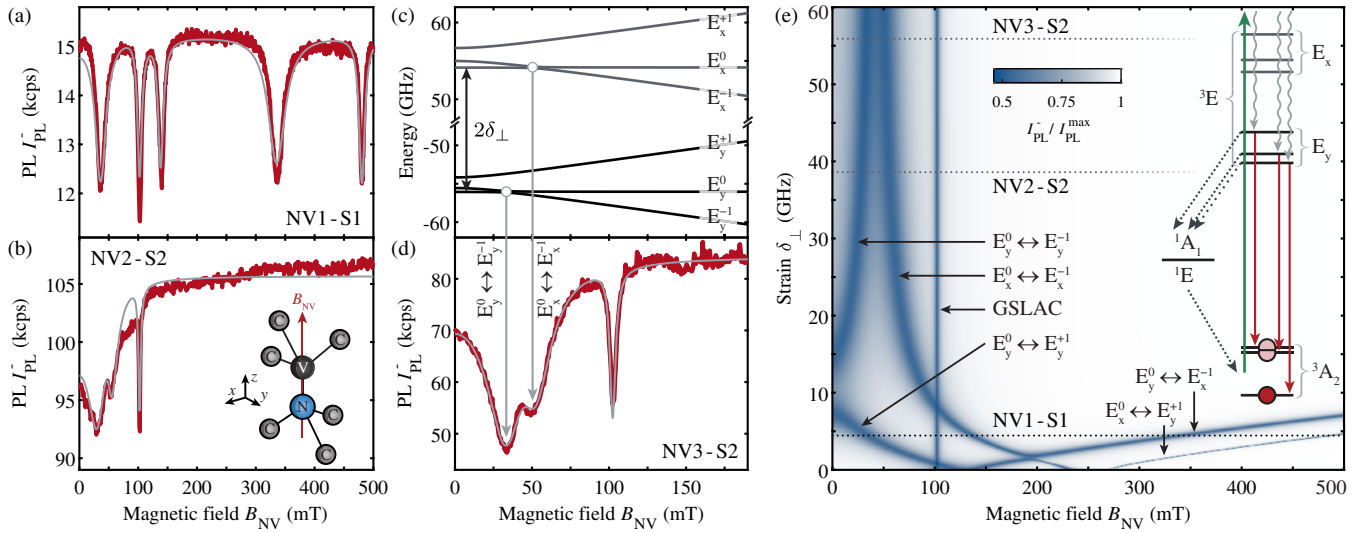

FIG. 1. (a) The NV$^-$ photoluminescence (PL) signal, I_{PL}^-, as a function of magnetic field, B_{NV}, for a typical "low strain" NV, NV1-$S1$ [transverse strain parameter $\delta_\perp = 4.444(3)$ GHz]. (b) Same as (a), but for an NV center exhibiting more strain [$\delta_\perp = 38.6(7)$ GHz]. The common I_{PL}^- dip at $B_{NV} = 102.4$ mT in (a) and (b) originates from the well-known ground-state level anticrossing (GSLAC), while additional dips result from excited-state level anticrossings (ESLACs). Gray lines are fits to our model (see text and [25]). All data were recorded at a temperature $T \approx 4$ K. (c) Example of NV$^-$ excited state energies for an NV experiencing even higher strain [$\delta_\perp = 55.9$ GHz]. Labels indicate the orbital- and spin degree of freedom of the states. (d) B_{NV} dependence of I_{PL}^- for NV3-$S2$ with $\delta_\perp = 55.9(6)$ GHz. The vertical arrows assign the observed I_{PL}^- dips to the corresponding ESLACs shown in (c). (e) PL intensity I_{PL}^- as a function of B_{NV} and $\delta_\perp$, calculated from a classical rate equation model for the ten-level system illustrated in (e) (for details, see [25]). Labels in (e) indicate which ESLACs are responsible for the respective PL dips, while horizontal lines show the $\delta_\perp$ values for the NVs presented in panels (a), (b), and (d). Inset: electronic levels and transition pathways considered in simulating the magnetic field dependence of I_{PL}^-. The NV$^-$ excited state energies are illustrated for the limit of large strain.

reported values of g_l to be inconsistent with our observations for NVs experiencing high strain, suggesting a strain dependence of g_l. In addition, our results provide new insights into (i) the mechanisms of NV charge state conversion and (ii) the efficiency of NV spin-initialization and readout, which are valuable for efficient NV-based quantum sensing under cryogenic conditions.

Our experiments are performed using a confocal optical microscope with samples held at temperatures $T \approx 4$ K in a closed-cycle refrigerator with optical access and three-axis vector magnetic field control. Optical excitation is performed with green, continuous-wave laser excitation at power levels close to saturation of the NV's optical transition. For optical detection, we use an avalanche photodiode and appropriate color filters to detect PL predominantly stemming from the NV's negative charge state, NV$^-$, with corresponding PL photon count rates I_{PL}^-.

We first investigate individual NV centers in two (100)-oriented, single-crystal "electronic grade" diamonds (element six), grown by chemical vapor deposition. These two samples differ in the nature of their NVs: in sample $S1$, we study naturally occurring NV centers, several microns deep in the bulk, while in sample $S2$, $\sim$10 nm deep NVs have been created by $^{14}N^+$ ion implantation at 12 keV and subsequent annealing. These two types of NV defects were chosen for studying a broad range of local strain, which is known to be increased for NVs implanted close to the diamond surface [20]. To enhance NV PL collection efficiencies, diamond solid immersion lenses and nanopillars were structured on samples $S1$ and $S2$, respectively, with methods reported elsewhere [21–23].

Figures 1(a) and 1(b) show representative data of I_{PL}^- as a function of B_{NV}, for two NV centers, NV1-$S1$ and NV2-$S2$ (where NVk-Sl denotes the kth NV located in sample Sl). For both NVs, $I_{PL}^-(B_{NV})$ shows several distinct, narrow local minima ("dips") at specific values of B_{NV}. The prominent, narrow dip at $B_{NV} = 102.4$ mT results from the NV's well-known ground-state level anticrossing (GSLAC) [24] and is present for all NVs we investigated. Conversely, the multiple additional dips, which occur reproducibly for each NV, only at different values of B_{NV}, are thus far unaccounted for.

We attribute the observed I_{PL}^- dips (excluding the GSLAC) to ESLACs, which result in spin mixing and subsequent population shelving into the NV$^-$ singlet manifold. Figures 1(c) and 1(d) exemplify this concept for NV3-$S2$, where we show calculated NV$^-$ excited state energies [1,16,33] (described below) alongside a measurement of $I_{PL}^-(B_{NV})$ to illustrate the coalescence between two ESLACs and the associated I_{PL}^- dips.

To obtain further, quantitative insights, we employ an extended version of a classical rate-equation model of the NV's magnetic field-dependent photophysics [12,17], where we now explicitly take into account the full,

low-temperature excited state level structure of NV$^-$ [33] [see Fig. 1(e), inset, for the electronic states and population decay channels taken into account]. For our calculations, we fix all transition rates to literature values by Gupta *et al.* [34,35], and only leave the relevant parameters of the NV$^-$ excited state Hamiltonian as free variables. We note that while some of the excited state transition rates have a temperature dependence for $T < 20$ K [36], this predominately has little to no effect on the position and intensity of the PL dips.

The energy splittings of the NV$^-$ excited states sensitively depend on lattice strain transverse to the NV axis. Such strain can result from electric fields or crystal stress [33], which we combine into a single perpendicular strain parameter $\delta_\perp = \sqrt{\delta_x^2 + \delta_y^2}$, where $\delta_{x(y)}$ are the corresponding strain parameters along x and y [Fig. 1(b), inset]. We then calculate the NV ^3E state energies by the Hamiltonian [1]

$$\hat{H}_{ES} = \hat{H}_{FS} + h[\delta_x \hat{\sigma}_z + \delta_y \hat{\sigma}_x + \mu_B (g_l \hat{\sigma}_y + g_e \hat{S}_z) B_{\mathrm{NV}}], \qquad (1)$$

where $\hat{H}_{FS}$ is the fine structure Hamiltonian of the ^3E manifold [1], h is Planck's constant, $\hat{\sigma}_i$ are the Pauli matrices representing the excited state orbital operators in the basis $\{E_x, E_y\}$ (the eigenstates of $\hat{H}_{ES}$ in the limit $\delta_\perp \gg \|\hat{H}_{FS}\|$), $\hat{S}_z$ is the $S = 1$ spin operator along the z axis, $\mu_B = 28$ GHz/T is the Bohr magneton and $g_{l(e)}$ is the orbital (electron) g factor ($g_e = 2.01$ [1]). Figure 1(e) shows the resulting model prediction of $I_{\mathrm{PL}}^-(B_{\mathrm{NV}})$ for varying $\delta_\perp$, and shows the strong dependence of the various I_{PL}^- dip locations on $\delta_\perp$. This explains the strongly varying $I_{\mathrm{PL}}^-(B_{\mathrm{NV}})$ traces we observe between different NVs, which naturally experience different levels of $\delta_\perp$. Conversely, a measurement of $I_{\mathrm{PL}}^-(B_{\mathrm{NV}})$ offers a sensitive tool to determine $\delta_\perp$ on the level of single NVs—a task that otherwise requires complex spectroscopic techniques [16].

We use our model to fit all $I_{\mathrm{PL}}^-(B_{\mathrm{NV}})$ data presented in this Letter, where gray lines overlaid on data show the resulting fits. For the fits we only left $\delta_\perp$, and a small misalignment angle in B_{NV} (and g_l in the case of NV1-*S*1—see below) as free parameters in Hamiltonian (1). In addition, we allow for scaling constants for contrast and normalization of I_{PL}^- and a parameter describing the relative excitation efficiency into orbitals E_x and E_y [15] to vary. All resulting fit parameters with errors are reported in [25]. We note that despite these few degrees of freedom, our model yields excellent fits for NVs experiencing a large range of strain values, from $\delta_\perp \lesssim \|\hat{H}_{FS}\|$ [Fig. 1(a)] to $\delta_\perp \gg \|\hat{H}_{FS}\|$ [Fig. 1(b)].

However, we observe significant deviations when studying $I_{\mathrm{PL}}^-(B_{\mathrm{NV}})$ for more highly strained NVs at elevated magnetic fields. There, our model predicts two additional I_{PL}^- dips [labeled $E^0_{x(y)} \leftrightarrow E^{\pm1}_{y(x)}$ in Fig. 1(e)], which arise from spin-mixing ESLACs between orbitals E_x and E_y.

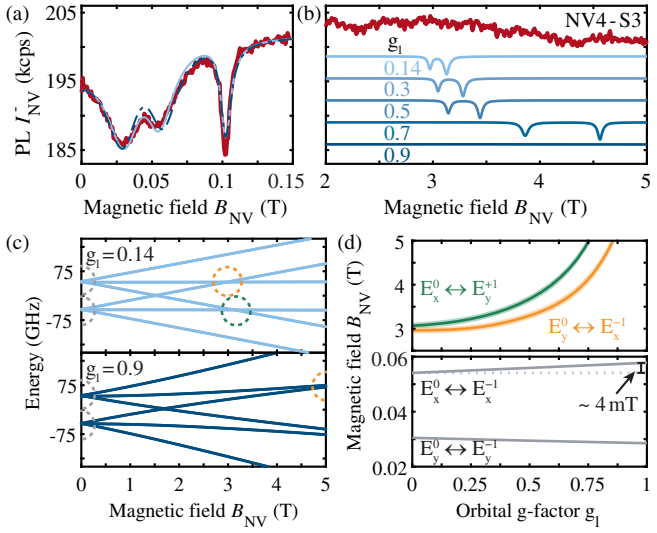

FIG. 2. (a) $I_{\mathrm{PL}}^-(B_{\mathrm{NV}})$ data (red) for NV4-*S*3 in the "low-field" regime ($B_{\mathrm{NV}} \lesssim 150$ mT). The model fit (blue) yields $\delta_\perp = 42.3(5)$ GHz and is largely unaffected by the value of g_l ($g_l = 0.14$ and 0.9; light and dark blue). (b) Same as (a) for stronger magnetic fields. Blue-shaded curves show model predictions (vertically offset for clarity) for $\delta_\perp = 42.3$ GHz and $g_l = 0.14, \ldots, 0.9$ (see labels). (c) Calculated ^3E excited state energies for $g_l = 0.14$ and $g_l = 0.9$. Dashed circles highlight the position of the $E_{x(y)} \leftrightarrow E_{y(x)}$ (green) and $E_{x(y)} \leftrightarrow E_{x(y)}$ (gray) ESLACs. (d) g_l dependence of the B_{NV} values at which various ESLACs occur. Shaded areas correspond to the propagated fitting errors in $\delta_\perp$ from (a).

To experimentally address this regime, we investigate single NV defects hosted in the (111)-oriented, electronic grade diamond *S*3 [23]. Figure 2(a) shows low-field $I_{\mathrm{PL}}^-(B_{\mathrm{NV}})$ data for the representative NV4-*S*3, where a fit (light blue) yields $\delta_\perp = 42.3(5)$ GHz [25], for which our model predicts the $E^0_{x(y)} \leftrightarrow E^{\pm1}_{y(x)}$ dips to occur at Tesla-range magnetic fields [Fig. 2(b), light blue]. Importantly, the $E^0_{x(y)} \leftrightarrow E^{\pm1}_{y(x)}$ dip location depends sensitively on g_l [blue traces in Figs. 2(b) and 2(c)], while the locations of the "low-field" I_{PL}^- dips shown in Fig. 2(a) are largely independent of g_l [Fig. 2(d)]. Conversely, an observation of the $E_{x(y)} \leftrightarrow E_{y(x)}$ LACs yields a sensitive determination of g_l on the level of single NVs. In the low strain regime (NV1-*S*1) we are able to extract the orbital g factor by fitting the position of the high field features, which results in $g_l = 0.1395$. In contrast, for NV4-*S*3 or any other NV we studied in sample *S*3, we were unable to observe the $E^0_{x(y)} \leftrightarrow E^{\pm1}_{y(x)}$ ESLACs, despite extensive experimental efforts; an observation which could be explained by an unexpected increase of g_l. Specifically, for the $\delta_\perp$ value of NV4-*S*3, $g_l \approx 0.8$ is the lowest value consistent with our observations [Fig. 2(d)], and we find similar conclusions for ~10 further NVs with comparable values of $\delta_\perp$, where we examined $I_{\mathrm{PL}}^-(B_{\mathrm{NV}})$ for B_{NV} up to 5 T [25].

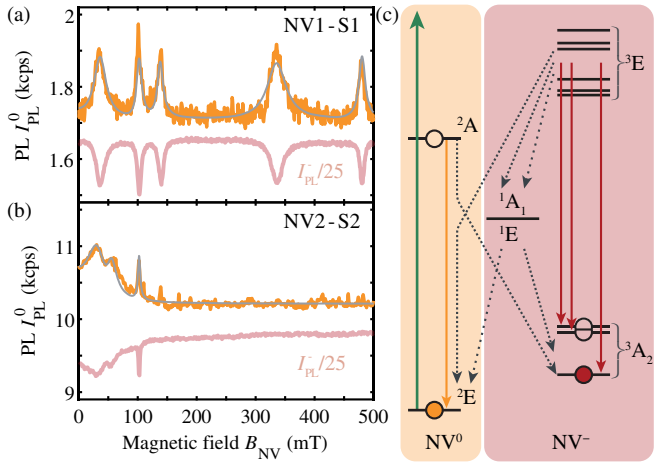

FIG. 3. (a) Magnetic field dependence of the NV^0 PL rate, $I^0_{PL}(B_{NV})$, for NV1-*S*1 and (b) NV2-*S*2, along with the corresponding I^-_{PL}-data [gray data points taken from Figs. 1(a) and 1(b), but rescaled for clarity]. Gray lines are theory predictions based on the fits shown in Figs. 1(a) and 1(b). (c) Electronic states of the NV^0-NV$^-$ system, with corresponding (de-)ionization rates, used to include charge-state dynamics into the model introduced in Fig. 1(f).

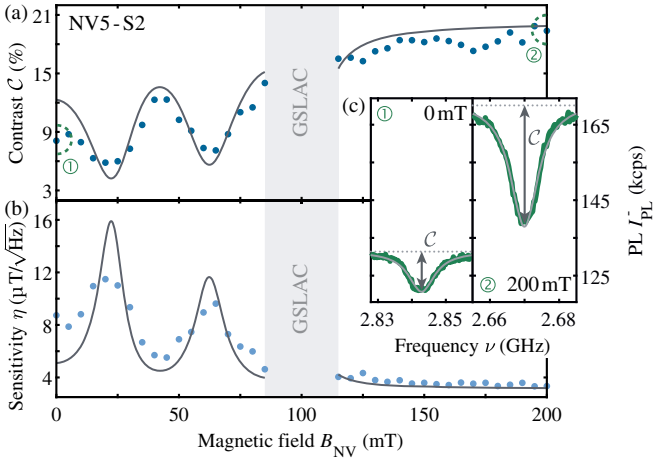

FIG. 4. (a) Dependence of the optically detected magnetic resonance (ODMR) contrast on magnetic field B_{NV} for NV5-*S*2. The microwave field amplitude (Rabi frequency) was held constant while varying B_{NV}. (b) Magnetic field dependence of the magnetic field sensitivity extracted from data (see text). Dark gray lines in (a) and (b) show theory predictions based on independently recorded $I^-_{PL}(B_{NV})$ data (see [25]). (c) Exemplary ODMR traces recorded at values of B_{NV} [dotted circles in (a)], where magnetic field sensitivity is strongly (left) and minimally (right) affected by excited state level anticrossings.

We note that this effect cannot be explained by a suppression of the mixing rate at higher strains. The mixing term for the $E^0_{x(y)} \leftrightarrow E^{\pm 1}_{y(x)}$ ESLACs is given by, $M_{E_xE_y} = d^{\perp}_{es}\delta_x\lambda^{\perp}_{es}/\sqrt{2}\sqrt{(d^{\perp}_{es}\delta_x)^2 + (B_z g_l \mu_B)^2}$, assuming only x-direction strain for simplicity. Importantly, this mixing term varies by $<1\%$ over the range of $B_z = 0$–0.5 T, and thus cannot explain the missing PL features. Likewise, phonon-induced orbital mixing between E_x and E_y can be ignored as the expected coupling rate is $\Gamma^{1-\mathrm{phon}} \approx 450$ kHz, which is significantly less than the other coupling rates considered, e.g., the intersystem crossing rate $\Gamma^{\mathrm{ICS}} > 10$ MHz and the state mixing rates $\Gamma^{\mathrm{mixing}} > 100$ MHz.

Our observations thus suggest a surprising, strain-induced enhancement of the orbital g factor of NV$^-$ over reported literature values $g_l \approx 0.1, \ldots, 0.22$ [17,37–39]. Such an effect has not been discussed in literature thus far, but can be made plausible by qualitative arguments. At low strain, the NV's orbital excited states are near degenerate, which allows for Jahn-Teller coupling to lead to a reduction of orbital angular momentum [38,40]. With increasing strain, the energy splitting of the states increases, which suppresses Jahn-Teller mixing, and thereby restores orbital angular momentum, leading to an increase of g_l toward the classical value $g_l = 1$. While a complete theoretical description of this suggested g_l enhancement is still lacking and beyond the scope of this Letter, we expect our findings to trigger further theoretical work on the topic.

The absence of the higher magnetic field features could also be explained by a time-dependent electric field from electrical noise near the NV spin, that would effectively smear out the features. This would indicate that there is a fluctuation of the electric field of greater than 1 kV/cm with a rate $\geq 1\,Hz$. Further measurements with improved time resolution would be required to separate these cases and will be pursued in future work.

Our method of monitoring I^-_{PL} versus B_{NV} also offers insights into the charge dynamics of the NV center. Specifically, we conducted experiments where we chose appropriate color filters [25] to record the PL intensity I^0_{PL} from the neutral charge state, NV^0 [Figs. 3(a) and 3(b)]. Strikingly, we find that all previously described I^-_{PL} dips are mirrored by peaks in I^0_{PL}. While the resulting buildup of NV^0 population remains small (and therefore only minimally affects our conclusions thus far), our model can be extended to include previously reported NV$^0 \leftrightarrow$ NV$^-$ (de)ionization processes [41,42] [Fig. 3(c)]. Importantly, within our model we can only explain the observed I^0_{PL} peaks by including a recently proposed [41], decay channel from the NV$^-$ singlet state ^1E to the ground state of NV^0—without this process our model yields dips instead of peaks in I^0_{PL}. Using the previously measured (de)ionization rates [41,42], our model then yields a quantitative prediction for $I^0_{PL}(B_{NV})$, without any free fit parameters, other than scaling constants for contrast and normalization of I^0_{PL} [gray lines in Figs. 3(a) and 3(b)].

The ESLAC induced dips in I^-_{PL} also have important implications for the magnetic-field sensitivity in low-temperature NV magnetometry. Indeed, the dips in I^-_{PL} are accompanied by corresponding dips in the spin readout

contrast $\mathcal{C}$ of optically detected magnetic resonance (ODMR) [43]. Figure 4(a) shows the evolution $\mathcal{C}(B_{\mathrm{NV}})$ for NV5-*S*2, while two exemplary ODMR traces recorded near and away from an I_{PL}^{-} dip ($B_{\mathrm{NV}} = 0$ and 200 mT, respectively) are shown in Fig. 4(c). This combined reduction in I_{PL}^{-} and $\mathcal{C}$ severely affect the NV's magnetic field sensitivity η. Using the well-established estimate [13,44] $\eta = (4/3\sqrt{3})(\Delta\nu/\gamma_{\mathrm{NV}}\mathcal{C}\sqrt{I_{\mathrm{PL}}^{-}})$, where $\Delta\nu$ is the ODMR linewidth, and $\gamma_{\mathrm{NV}} = 28$ GHz/T the NV's gyromagnetic ratio, we extract $\eta(B_{\mathrm{NV}})$ shown in Fig. 4(b). Compared to typical sensitivity values $\eta \approx 3\ \mu\mathrm{T/Hz}^{0.5}$ away from the ESLACs (e.g., at $B_{\mathrm{NV}} \approx 200$ mT), η drops by almost an order of magnitude on the I_{PL}^{-} dips.

For nanoscale NV magnetometry, which exploits near-surface NV centers for which we consistently find $\delta_{\perp} > 20$ GHz [Fig. 1(f)], this decrease of magnetometry performance predominantly affects magnetometry at $B_{\mathrm{NV}} \lesssim 100$ mT [c.f. Fig. 1(f)]. The fact that all such "shallow" NVs exhibit significant values of $\delta_{\perp}$ can be assigned to internal electric fields due to band bending near the diamond surface [20,45], or to near-surface crystal stress [46]. Magnetic field sensitivity for such NVs could in the future be restored by materials engineering to reduce $\delta_{\perp}$ near diamond surfaces, by working with NVs oriented normal to the diamond surface [47] or by harnessing the dependence of the I_{PL}^{-} dip depth on the excitation laser polarization [15,25]. Further improvements could be achieved by optimizing laser excitation powers or by exploiting resonant laser excitation where specific ESLACs could be avoided by choosing the proper laser excitation frequency. It is also possible to utilize these ESLACs to perform microwave free magnetometry and strain sensing, in a similar fashion to previous work with the NV GSLAC [48].

Our work on the low temperature magnetic field dependence of NV fluorescence rates offers a simple, yet precise and quantitative tool to characterize the excited state structure of individual NV centers. These findings not only offer insights into the NV center orbital structure and charge dynamics, but are also relevant to applications in quantum information processing and quantum sensing, where precise knowledge of the excited state structure is key. Exploring the temperature dependence of the I_{PL}^{-} dips would constitute a worthwhile extension to our work that might offer further insights into orbital averaging processes that dominate the NV's photophysics at elevated temperatures [15]. Importantly, the method we demonstrated and applied here is not limited to NV centers alone—the excited state structure of any color center exhibiting dark states that can be populated through magnetic field tunable ESLACs, such as the neutral silicon-vacancy center in diamond [49], could be investigated as well.

We gratefully acknowledge Ronald Hanson, Arian Stolk, and their colleagues for making sample *S*1 available for this study and Johannes Kölbl for help in creating the figures. We further acknowledge financial support through the NCCR QSIT (Grant No. 185902), the Swiss Nanoscience Institute, the EU Quantum Flagship Project ASTERIQS (Grant No. 820394), and through the Swiss NSF Project Grant No. 188521.

*patrick.maletinksy@unibas.ch

[1] M. W. Doherty, N. B. Manson, P. Delaney, F. Jelezko, J. Wrachtrup, and L. C. L. Hollenberg, Phys. Rep. **528**, 1 (2013).
[2] C. L. Degen, F. Reinhard, and P. Cappellaro, Rev. Mod. Phys. **89**, 035002 (2017).
[3] F. Casola, T. van der Sar, and A. Yacoby, Nat. Rev. Mater. **3**, 17088 (2018).
[4] N. Kalb, A. A. Reiserer, P. C. Humphreys, J. J. W. Bakermans, S. J. Kamerling, N. H. Nickerson, S. C. Benjamin, D. J. Twitchen, M. Markham, and R. Hanson, Science **356**, 928 (2017).
[5] D. M. Toyli, D. J. Christle, A. Alkauskas, B. B. Buckley, C. G. Van de Walle, and D. D. Awschalom, Phys. Rev. X **2**, 031001 (2012).
[6] Kai-Mei C. Fu, G. Z. Iwata, A. Wickenbrock, and D. Budker, AVS Quantum Sci. **2**, 044702 (2020).
[7] B. Hensen, H. Bernien, A. E. Dreau, A. Reiserer, N. Kalb, M. S. Blok, J. Ruitenberg, R. F. L. Vermeulen, R. N. Schouten, C. Abellan, W. Amaya, V. Pruneri, M. W. Mitchell, M. Markham, D. J. Twitchen, D. Elkouss, S. Wehner, T. H. Taminiau, and R. Hanson, Nature (London) **526**, 682 (2015).
[8] L. Rondin, J.-P. Tetienne, T. Hingant, J.-F. Roch, P. Maletinsky, and V. Jacques, Rep. Prog. Phys. **77**, 056503 (2014).
[9] L. Thiel, D. Rohner, M. Ganzhorn, P. Appel, E. Neu, B. Müller, R. Kleiner, D. Koelle, and P. Maletinsky, Nat. Nanotechnol. **11**, 677 (2016).
[10] L. Thiel, Z. Wang, M. A. Tschudin, D. Rohner, I. Gutierrez-Lezama, N. Ubrig, M. Gibertini, E. Giannini, A. F. Morpurgo, and P. Maletinsky, Science **364**, 973 (2019).
[11] J. Harrison, M. J. Sellars, and N. B. Manson, J. Lumin. **107**, 245 (2004).
[12] J.-P. Tetienne, L. Rondin, P. Spinicelli, M. Chipaux, T. Debuisschert, J.-F. Roch, and V. Jacques, New J. Phys. **14**, 103033 (2012).
[13] A. Dréau, M. Lesik, L. Rondin, P. Spinicelli, O. Arcizet, J. F. Roch, and V. Jacques, Phys. Rev. B **84**, 195204 (2011).
[14] M. Steiner, P. Neumann, J. Beck, F. Jelezko, and J. Wrachtrup, Phys. Rev. B **81**, 035205 (2010).
[15] Kai-Mei C. Fu, C. Santori, P. E. Barclay, L. J. Rogers, N. B. Manson, and R. G. Beausoleil, Phys. Rev. Lett. **103**, 256404 (2009).
[16] A. Batalov, V. Jacques, F. Kaiser, P. Siyushev, P. Neumann, L. J. Rogers, R. L. McMurtrie, N. B. Manson, F. Jelezko, and J. Wrachtrup, Phys. Rev. Lett. **102**, 195506 (2009).
[17] L. J. Rogers, R. L. McMurtrie, M. J. Sellars, and N. B. Manson, New J. Phys. **11**, 063007 (2009).

[18] M. Pompili, S. L. Hermans, S. Baier, H. K. Beukers, P. C. Humphreys, R. N. Schouten, R. F. Vermeulen, M. J. Tiggelman, L. dos Santos Martins, B. Dirkse, S. Wehner, and R. Hanson, Science **372**, 259 (2021).
[19] S. E. Lillie, D. A. Broadway, N. Dontschuk, S. C. Scholten, B. C. Johnson, S. Wolf, S. Rachel, L. C. L. Hollenberg, and J.-P. Tetienne, Nano Lett. **20**, 1855 (2020).
[20] D. A. Broadway, N. Dontschuk, A. Tsai, S. E. Lillie, C. T.-K. Lew, J. C. McCallum, B. C. Johnson, M. W. Doherty, A. Stacey, L. C. L. Hollenberg, and J.-P. Tetienne, Natl. Electron. Rev. **1**, 502 (2018).
[21] N. Hedrich, D. Rohner, M. Batzer, P. Maletinsky, and B. J. Shields, Phys. Rev. Applied **14**, 064007 (2020).
[22] L. Robledo, L. Childress, H. Bernien, B. Hensen, P. F. A. Alkemade, and R. Hanson, Nature (London) **477**, 574 (2011).
[23] E. Neu, P. Appel, M. Ganzhorn, J. Miguel-Sánchez, M. Lesik, V. Mille, V. Jacques, A. Tallaire, J. Achard, and P. Maletinsky, Appl. Phys. Lett. **104**, 153108 (2014).
[24] A. Wickenbrock, H. Zheng, L. Bougas, N. Leefer, S. Afach, A. Jarmola, V. M. Acosta, and D. Budker, Appl. Phys. Lett. **109**, 053505 (2016).
[25] See Supplemental Material at http://link.aps.org/supplemental/10.1103/PhysRevLett.128.177401 for further discussions, which include [26–32].
[26] L. Robledo, H. Bernien, T. van der Sar, and R. Hanson, New J. Phys. **13**, 025013 (2011).
[27] P. Appel, E. Neu, M. Ganzhorn, A. Barfuss, M. Batzer, M. Gratz, A. Tschöpe, and P. Maletinsky, Rev. Sci. Instrum. **87**, 063703 (2016).
[28] A. Tallaire, J. Achard, A. Boussadi, O. Brinza, A. Gicquel, I. Kupriyanov, Y. Palyanov, G. Sakr, and J. Barjon, Diam. Relat. Mater. **41**, 34 (2014).
[29] M. Lesik, J.-P. Tetienne, A. Tallaire, J. Achard, V. Mille, A. Gicquel, J.-F. Roch, and V. Jacques, Appl. Phys. Lett. **104**, 113107 (2014).
[30] K. J. Brown, E. Chartier, E. M. Sweet, D. A. Hopper, and L. C. Bassett, J. Chem. Health Safety **26**, 40 (2019).
[31] V. Jacques, P. Neumann, J. Beck, M. Markham, D. Twitchen, J. Meijer, F. Kaiser, G. Balasubramanian, F. Jelezko, and J. Wrachtrup, Phys. Rev. Lett. **102**, 057403 (2009).
[32] M. L. Goldman, M. W. Doherty, A. Sipahigil, N. Y. Yao, S. D. Bennett, N. B. Manson, A. Kubanek, and M. D. Lukin, Phys. Rev. B **91**, 165201 (2015).
[33] J. R. Maze, A. Gali, E. Togan, Y. Chu, A. Trifonov, E. Kaxiras, and M. D. Lukin, New J. Phys. **13**, 025025 (2011).
[34] A. Gupta, L. Hacquebard, and L. Childress, J. Opt. Soc. Am. B **33**, B28 (2016).
[35] We note that our main findings are insensitive to the rates employed and we find largely identical results by employing other literature values.
[36] M. L. Goldman, A. Sipahigil, M. W. Doherty, N. Y. Yao, S. D. Bennett, M. Markham, D. J. Twitchen, N. B. Manson, A. Kubanek, and M. D. Lukin, Phys. Rev. Lett. **114**, 145502 (2015).
[37] N. Reddy, N. Manson, and E. Krausz, J. Lumin. **38**, 46 (1987).
[38] D. Braukmann, E. R. Glaser, T. A. Kennedy, M. Bayer, and J. Debus, Phys. Rev. B **97**, 195448 (2018).
[39] H. Hanzawa, H. Nishikori, Y. Nisida, S. Sato, T. Nakashima, S. Sasaki, and N. Miura, Physica (Amsterdam) **184B**, 137 (1993).
[40] D. Braukmann, Optical properties of vacancies in diamond at high magnetic fields, Ph.D. thesis, TU Dortmund University, Germany, 2018.
[41] D. P. L. Aude Craik, P. Kehayias, A. S. Greenspon, X. Zhang, M. J. Turner, J. M. Schloss, E. Bauch, C. A. Hart, E. L. Hu, and R. L. Walsworth, Phys. Rev. Applied **14**, 014009 (2020).
[42] N. Aslam, G. Waldherr, P. Neumann, F. Jelezko, and J. Wrachtrup, New J. Phys. **15**, 013064 (2013).
[43] A. Gruber, A. Drabenstedt, C. Tietz, L. Fleury, J. Wrachtrup, and C. Borczyskowski, Science **276**, 2012 (1997).
[44] J. F. Barry, J. M. Schloss, E. Bauch, M. J. Turner, C. A. Hart, L. M. Pham, and R. L. Walsworth, Rev. Mod. Phys. **92**, 015004 (2020).
[45] A. Stacey, N. Dontschuk, J.-P. Chou, D. A. Broadway, A. K. Schenk, M. J. Sear, J.-P. Tetienne, A. Hoffman, S. Prawer, C. I. Pakes, A. Tadich, N. P. de Leon, A. Gali, and L. C. L. Hollenberg, Adv. Mater. Interfaces **6**, 1801449 (2019).
[46] D. J. McCloskey, N. Dontschuk, D. A. Broadway, A. Nadarajah, A. Stacey, J. P. Tetienne, L. C. Hollenberg, S. Prawer, and D. A. Simpson, ACS Appl. Mater. Interfaces **12**, 13421 (2020).
[47] D. Rohner, J. Happacher, P. Reiser, M. A. Tschudin, A. Tallaire, J. Achard, B. J. Shields, and P. Maletinsky, Appl. Phys. Lett. **115**, 192401 (2019).
[48] H. Zheng, Z. Sun, G. Chatzidrosos, C. Zhang, K. Nakamura, H. Sumiya, T. Ohshima, J. Isoya, J. Wrachtrup, A. Wickenbrock, and D. Budker, Phys. Rev. Applied **13**, 044023 (2020).
[49] Z.-H. Zhang, P. Stevenson, G. m. H. Thiering, B. C. Rose, D. Huang, A. M. Edmonds, M. L. Markham, S. A. Lyon, A. Gali, and N. P. de Leon, Phys. Rev. Lett. **125**, 237402 (2020).